Proceedings of ASME Turbo Expo 2011
GT2011
June 6-10, 2011, Vancouver, British Columbia, Canada

GT2011-46561

LARGE EDDY SIMULATION OF FLOW AND CONVECTIVE HEAT TRANSFER IN A GAS TURBINE CAN COMBUSTOR WITH SYNTHETIC INLET TURBULENCE

Sunil Patil
Virginia Tech
Blacksburg, Virginia, USA

Danesh Tafti
Virginia Tech
Blacksburg, Virginia, USA

ABSTRACT

Large eddy simulations of swirling flow and the associated convective heat transfer in a gas turbine can combustor under cold flow conditions for Reynolds numbers of 50,000 and 80,000 with characteristic Swirl number of 0.7 are carried out. A precursor Reynolds Averaged Navier-Stokes (RANS) simulation is used to provide the inlet boundary conditions to the large-eddy simulation (LES) computational domain, which includes only the can combustor. A stochastic procedure based on the classical view of the turbulence as superposition of the coherent structures is used to simulate the turbulence at the inlet plane of the computational domain using the mean flow velocity and Reynolds stress data from the precursor RANS simulation. To further reduce the overall computational resource requirement and the total computational time, the near wall region is modeled using zonal two layer model. A novel formulation in generalized co-ordinate system is used for solution of effective tangential velocity and temperature in the inner layer virtual mesh. LES predictions are compared with the experimental data of Patil et al. [1] for the local heat transfer distribution on the combustor liner wall obtained using robust infrared thermography technique. The heat transfer coefficient distribution on the liner wall predicted from LES is in good agreement with experimental values. The location and the magnitude of the peak heat transfer are predicted in very close agreement with the experiments.

1 INTRODUCTION

Modern gas turbine combustors are characterized by highly swirling and expanding flows that makes the convective heat load on the gas side difficult to predict and estimate. Both the desire for better efficiency and the need for lower emissions have reduced the amount of cooling air that the combustion engineer has available for combustor liner cooling. As combustors are designed to reduce emissions, there is insufficient liner cooling available as more air is utilized in the premixing process and reaction zones to maintain as low a temperature as possible. To avoid liner failure from over-heating, it is extremely important to quantify the liner heat load accurately in the lean premixed combustor environment. Measurements using hot wire anemometry, particle image velocimetry (PIV) and laser Doppler velocimetry (LDV) have been reported on confined swirl flows [2-7]. There are very few studies performed to characterize the heat transfer on the combustor liner wall at realistic engine condition Reynolds number. Patil et al. [1] recently measured and predicted heat transfer coefficient on the combustor liner wall at realistic high Reynolds numbers in industrial gas turbine combustor geometries. Experiments can only provide limited data in such a flowfield due to practical limitations but accurate numerical calculations can provide a deeper characterization of many three dimensional complex flow features. But turbulent swirling flows, which are characterized by high strain rates and highly anisotropic turbulence, are difficult to simulate numerically. Several researchers [1, 4-6, 8] have reported Reynolds-averaged Navier-Stokes (RANS) studies on wall bounded swirling flows. Other approaches such as large-eddy simulations (LES) have the potential of providing a more physical basis for simulations.

A limited number of studies have been reported in the literature on LES of swirling flows. Grinstein and Fureby [9] presented LES of non-reacting as well as reacting flow in a lean premixed low NO_x model gas turbine combustor and obtained reasonable agreement with experiments. Wang et al. [10] explored various aspects of swirling flow development such as, the central recirculating flow, the precessing vortex core, and the Kelvin-Helmholtz instability in a gas turbine injector. Pierce and Moin [11] investigated a low Swirl number case and obtained promising agreement with experiments, while Kim et al. [12] performed a reactive flow calculation for a high Swirl number case.

Although LES only resolves the large-scale unsteady flow dynamics in complex flows, it requires large computational resources at practical Reynolds number, which are of order of several hundred thousand in gas turbine combustors. Resolution requirements near the wall increase tremendously with Reynolds number [13]. In wall bounded flows, the number of computational cells required to resolve the energy producing structures in the near-wall region scale as Re^2. Hence, it is crucial to reduce the high resolution requirement for successful implementation of LES at high Reynolds numbers. Modeling the near wall region and coupling it to the outer LES region is key to the use of LES for practical engineering applications.

Three approaches for modeling the near wall layer are the use of logarithmic law of the wall based functions, solving a separate set of equations in the near-wall region and simulating this region in Reynolds-averaged sense. Deardorff [14] and Schumann [15] introduced wall models based on equilibrium between pressure and viscous forces. Grotzbach [16], Werner and Wengle [17], Piomelli et al. [18], Hoffmann and Benocci [19], and Temmerman et al. [20] used different variants of this approach. The major drawback of this approach is that it needs a value of the mean wall shear stress *a priori* and the plane averaged velocity at the first grid point off the wall has to explicitly satisfy the logarithmic law of the wall. Hence, Schumann's [15] model and its variants work well only in simple equilibrium flows like the fully developed channel and pipe flows.

In recent years, the hybrid RANS-LES approach has caught the attention of many researchers in which RANS equations are solved near the wall while the LES filtered Navier-Stokes equations are solved away from the wall. Various methodologies are used to switch between the RANS and LES. Spalart et al. [21] proposed Detached Eddy Simulation (DES) for separated flows in which a characteristic turbulent length scale was used as a criterion to switch between the RANS and LES regions. Nikitin et al. [22] used Spalart et al. [21] model and found significant under prediction in the wall shear stress in turbulent channel flow. These hybrid RANS-LES models have the capability to simulate complex flows but still suffer from a high grid resolution requirement in the wall normal direction, which require $y^+<1$. Compatibility of the turbulence conditions at the interface and aliasing effects due to the resolved and modeled turbulence are major challenges in this method. In spite of these issues, this method has been applied to a number of complex flows with good results [23].

The zonal model or two-layer model (TLM) on the other hand solves a different set of equations in the inner wall layer [24]. Simplified turbulent boundary layer equations are solved on a virtual grid set up in the wall layer. This grid is embedded in the outer LES grid and refined only in the wall normal direction. In the outer LES grid, the filtered Navier-Stokes equations are solved, while in the inner layer Equation (1) is solved on a virtual grid embedded between the first grid point off the wall and the wall.

$$\frac{\partial \bar{u}_i}{\partial t}+\frac{\partial}{\partial x_i}\left(\bar{u}_n\bar{u}_i\right)=-\frac{1}{\rho}\frac{\partial \bar{p}}{\partial x_i}+\frac{\partial}{\partial x_n}\left[\left(\nu+\nu_t\right)\frac{\partial \bar{u}_i}{\partial x_n}\right] \qquad (1)$$

In Equation (1), n is the wall normal direction and i takes values 1, 2 or 1, 3 based on the wall orientation. The wall normal velocity u_n is computed using mass conservation in the inner layer. Equation (1) is solved using the no-slip boundary condition at the wall, and the velocity at the first grid point off the wall, which is calculated from the outer-flow LES. The wall-stress components in the streamwise and spanwise directions, obtained from the integration of Equation (1) in the inner layer are used as the boundary conditions for the outer-flow LES calculation. This procedure is costlier than the equilibrium wall models but still very inexpensive compared to the wall layer resolved LES because the inner layer calculations take a very small percentage of the total cost of the whole calculation. Also the pressure Poisson-equation need not be solved in the inner layer as the pressure field just outside the inner layer is imposed on the inner layer. Also , this procedure do not explicitly depend on logarithmic law of the wall to obtain wall shear stress as in case of wall function approach with or without pressure gradient[24]. Balaras and Benocci [24] and Balaras et al. [25] used an algebraic eddy viscosity model to parameterize all scales of motion in the wall layer. The zonal model is discussed in more detail in the next section. The zonal approach has been successfully applied to a variety of problems in recent years. Cabot and Moin [26] simulated the flow over a backward facing step, Wang and Moin [27] studied flow past an asymmetric trailing edge, and Tessicini et al. [28] simulated the three-dimensional flow around a hill-shaped obstruction with the zonal near wall approach. In all these applied schemes, turbulent boundary layer equations are solved in the inner layer virtual mesh to obtain the instantaneous wall shear stress, which is fed back as a boundary condition to the outer LES region. Most of the applications of wall layer modeling in LES framework have been applied to fluid flow problems without heat transfer. In the current study, zonal treatment for the near wall heat transfer for coarser meshes is presented. The zonal two layer model for velocity and temperature is integrated and formulated to account for Dirichlet as well as Neumann boundary conditions at the wall. A thorough validation of the proposed formulation is done by Patil and Tafti [29] in a fully developed turbulent channel flow against well resolved LES calculations. Patil and Tafti [29] also applied this methodology to investigate the fully developed flow and heat transfer in a square ribbed duct used for gas turbine bade cooling.

Another major challenge in the simulation of complex wall bounded turbulent flows is the accurate specification of the turbulent inlet boundary condition. For direct numerical simulations (DNS) and LES simulating highly turbulent flows, specifications of inlet flow data is critical. In unsteady LES computations, it is required that the inlet data should have time and space dependent velocity signals representative of the inflow turbulence. It is also desired that the inflow boundaries in spatially evolving flows be placed as close to regions of interest as possible to reduce the computational effort. This makes accurate specification of inflow data even more critical as predictions downstream depend heavily on it.

The most accurate method for specifying the instantaneous velocity fluctuation for LES or DNS is to run a precursor simulation. These precursor simulations can use periodic boundary conditions in the streamwise direction. The time-dependent flow field is then scaled to satisfy the requirements of the actual simulation. Kaltenbach et al. [30] and Friedrich and Arnal [31] used the velocity profiles extracted from planes in a precursor periodic channel flow to generate inflow data for a LES of a plane diffuser and a backward-facing step, respectively. This method requires significant amount of computational resources and storage space and leads to the introduction of artificial modes caused by recycling a finite number of frames [32]. Hence, there is a need to develop a generic method to simulate inlet turbulence synthetically without resorting to additional precursor simulations.

Lund et al. [33] proposed a rescaling/recycling method for generating inlet conditions for a zero pressure gradient boundary layer. This method uses the velocity in a plane several boundary layer thicknesses downstream of the inlet (the rescaling station) to calculate the velocity signal at the inlet plane. At the rescaling station, the velocity field is decomposed into a mean and fluctuating part. Then the rescaled velocity is taken as a boundary condition at the inlet. Lund et al. [33] have shown that this procedure results in a spatially evolving boundary layer simulation that generates its own inflow data. Planes of velocity data can be saved from precursor simulations using this procedure and then used as an inflow boundary condition for the main simulation. Aider and Danet [34] used this procedure to generate inlet conditions for turbulent flow over a backward-facing step. Wang and Moin [35] generated inlet conditions for a hydrofoil upstream of the trailing edge using the same procedure. Sagaut et al. [36] extended this procedure to compressible flows. The method used in this study for simulating the inlet turbulence is a based on the work of Jarrin et al. [37]. This method is based on generating coherent structures in the inlet plane of the computational domain defined by a kernel shape function based on the integral length scale. The method is briefly described in the next section.

The paper combines two important components needed for the simulation of high Reynolds number turbulent flows in complex geometries, namely, wall layer modeling and inlet turbulence generation, both of which have a large impact on reducing computational complexity. Flow through an engine scale swirler and model can combustor of an industrial gas turbine is studied. The RANS data of Patil et al. [1], validated against experimental data is used to provide inflow conditions for large-eddy simulations. A stochastic method based on the classical view of turbulence as superposition of coherent structures is used to simulate the turbulence at the inlet plane. A novel formulation is used for inner layer computations near the wall. Two different Reynolds numbers, 50,000 and 80,000, based on the hydraulic diameter of the can combustor and the bulk mean combustor velocity are investigated. The near wall zonal treatment results in less computational resources and a lot less overall computational time at these high Reynolds numbers. This is the first hybrid RANS LES study performed in a realistic gas turbine configuration where the synthetic eddy method is used at the interface between the two. It is shown that predictions with large-eddy simulations using synthetic inlet turbulence are able to accurately represent the complex swirling flow features inside the gas turbine combustor at high Reynolds number and predicts the liner wall heat transfer accurately. This is also the first study where an integrated zonal near wall treatment for velocity and temperature is used in a generalized coordinates LES framework system to characterize the combustor liner wall heat transfer at high Reynolds numbers.

2 COMPUTATIONAL METHODOLOGY

2.1 Governing equations

The governing equations for unsteady incompressible viscous flow in a generalized coordinate system consists of mass, momentum, and energy conservation laws. The equations are mapped from physical $(\vec{x})$ to logical/computational space $(\vec{\xi})$ by a boundary conforming transformation $\vec{x} = \vec{x}(\vec{\xi})$, where $\vec{x} = (x, y, z)$ and $\vec{\xi} = (\xi, \eta, \zeta)$. The equations are non-dimensionalized by a suitable length scale (L^*) and velocity scale (U^*). For industrial scale can combustor investigated in current paper, length scale is chosen as hydraulic diameter of the combustor ($L^*=D=0.203$m) and velocity scale is chosen as bulk mean combustor velocity ($U^*=U_b$). The governing equations are written in conservative non-dimensional form as:

<u>Mass</u>:

$$\frac{\partial}{\partial \xi_j}\left(\sqrt{g}U^j\right) = 0 \tag{2}$$

<u>Momentum</u>:

$$\frac{\partial}{\partial t}\left(\sqrt{g}u_i\right) + \frac{\partial}{\partial \xi_j}\left(\left(\sqrt{g}U^j\right)u_i\right) = -\frac{\partial}{\partial \xi_j}\left(\sqrt{g}\,(\vec{a}^{\,j})_i\, p\right) + \frac{\partial}{\partial \xi_j}\left(\left(\frac{1}{\mathrm{Re}} + \frac{1}{\mathrm{Re}_t}\right)\sqrt{g}\,g^{jk}\frac{\partial u_i}{\partial \xi_k}\right) \tag{3}$$

<u>Energy:</u>

$$\frac{\partial}{\partial t}\left(\sqrt{g}\theta\right) + \frac{\partial}{\partial \xi_j}\left(\left(\sqrt{g}U^j\right)\theta\right) = \frac{\partial}{\partial \xi_j}\left(\left(\frac{1}{\mathrm{Re}\,\mathrm{Pr}} + \frac{1}{\mathrm{Re}_t\,\mathrm{Pr}_t}\right)\sqrt{g}\,g^{jk}\frac{\partial u_i}{\partial \xi_k}\right) \tag{4}$$

where $\vec{a}^i$ are the contravariant basis vectors, $\sqrt{g}$ is the Jacobian of the transformation, g^{ij} is the contravariant metric tensor, $\sqrt{g}U^j = \sqrt{g}\left(\vec{a}^j\right)_k u_k$ is the contravariant flux vector, u_i is the Cartesian velocity vector, p is the pressure, and θ is the non-dimensional temperature ($\theta = \dfrac{T - T_{ref}}{T_0}; T_0 = \dfrac{q_w^{"} L^*}{k}$). The non-dimensional time used is t^*U^*/L^* and the Reynolds number is given by U^*L^*/ν, Re_t is the inverse of the subgrid eddy-viscosity, which is modeled as

$$\frac{1}{\mathrm{Re}_t} = C_s^{\,2}(\sqrt{g})^{2/3}\left|\bar{S}\right| \tag{5}$$

where $\left|\bar{S}\right|$ is the magnitude of the strain rate tensor given by $\left|\bar{S}\right| = \sqrt{2\overline{S_{ik}}\,\overline{S_{ik}}}$ and the Smagorinsky constant $C_s^{\,2}$ is obtained via the dynamic subgrid stress model [38]. To this end, a second test filter, denoted by $\hat{G}$, is applied to the filtered governing equations with the characteristic length scale of $\hat{G}$ being larger than that of the grid filter, $\bar{G}$. The test filtered quantity is obtained from the grid filtered quantity by a second-order trapezoidal filter, which is given by $\hat{\varphi} = \frac{1}{4}(\bar{\varphi}_{i-1} + 2\bar{\varphi}_i + \bar{\varphi}_{i+1})$ in one dimension. The resolved turbulent stresses, representing the energy scales between the test and grid filters, $L_{ij} = \widehat{\bar{u}_i\bar{u}_j} - \hat{\bar{u}}_i\hat{\bar{u}}_j$, are then related to the subtest, $T_{ij} = \widehat{\overline{u_i u_j}} - \hat{\bar{u}}_i\hat{\bar{u}}_j$, and subgrid-scales stresses $\tau_{ij} = \overline{u_i u_j} - \overline{u}_i\overline{u}_j$ through the identity, $L_{ij}^a = T_{ij}^a - \hat{\tau}_{ij}^a$. The anisotropic subgrid and subtest-scale stresses are then formulated in terms of the Smagorinsky eddy viscosity model as:

$$\widehat{\tau_{ij}^a} = -2C_s^2\left(\sqrt{g}\right)^{2/3}\widehat{\left|\bar{S}\right|\overline{S_{ij}}} \tag{6}$$

$$T_{ij}^a = -2C_s^{\,2}\alpha\left(\sqrt{g}\right)^{2/3}\left|\hat{\bar{S}}\right|\widehat{\overline{S_{ij}}} \tag{7}$$

using the identity,

$$\begin{aligned}\widehat{L_{ij}^a} = \widehat{L}_{ij} - \frac{1}{3}\delta_{ij}L_{kk} &= 2C_s^2\left(\sqrt{g}\right)^{2/3}\left[\alpha\left|\hat{\bar{S}}\right|\widehat{\overline{S_{ij}}} - \widehat{\left|\bar{S}\right|\overline{S_{ij}}}\right] \\ &= -2C_s^2\left(\sqrt{g}\right)^{2/3}M_{ij}\end{aligned} \tag{8}$$

Here α is the square of the ratio of the characteristic length scale associated with the test filter to that of grid filter and is taken to be $\left[\widehat{\Delta}_i / \overline{\Delta}_i = \sqrt{6}\right]$ for a representative one-dimensional test filtering operation . Using a least-squares minimization procedure of Lilly [39], a final expression for $C_s^{\,2}$ is obtained as:

$$C_s^{\,2} = -\frac{1}{2}\frac{1}{(\sqrt{g})^{2/3}}\frac{L_{ij}^a \bullet M_{ij}}{M_{ij} \bullet M_{ij}} \tag{9}$$

The value of $C_s^{\,2}$ is constrained to be positive by setting it to zero when $C_s^{\,2} < 0$.

2.2 Zonal two layer flow model

The zonal two layer model formulation in the generalized coordinate system (ξ, η, ζ) is described in this section briefly in a very simplified form.

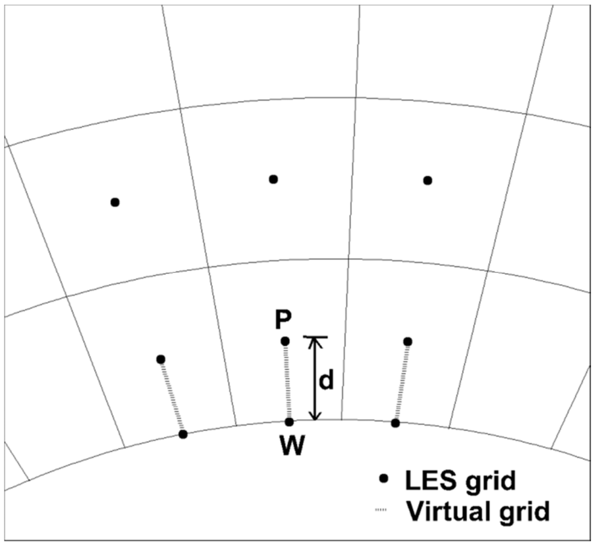

Figure 1: Virtual grid for wall model, embedded in LES grid (W represent wall node. P represent first off wall LES grid node)

Figure 1 shows the virtual grid in the wall normal direction required for the two layer wall model embedded in the outer LES grid. Simplified turbulent boundary layer equations of form described by Equation (1) are solved on this virtual grid. Instead of using (x,y,z) or (ξ, η, ζ) coordinate systems, a coordinate system of reduced dimensionality (t,n) is used where t is the tangential and n is the normal direction to the wall. Neglecting the unsteady and convection terms on the LHS of Equation (1), it can be written as

$$\frac{\partial}{\partial n}\left[\left(\frac{1}{\mathrm{Re}} + \frac{1}{\mathrm{Re}_t}\right)\frac{\partial u_t}{\partial n}\right] = \frac{\partial P}{\partial t} \tag{10}$$

The Cartesian components of the velocity vector at the first nodal point off the wall are used to find the tangential velocity (U_t), which serves as the boundary condition for the inner layer. Similarly, the pressure gradient in the tangential velocity direction $(\partial P / \partial t)$ is also calculated using the outer LES and is assumed constant in the inner layer. Equation (10) is solved on an embedded virtual grid in the wall normal direction with a no-slip boundary condition at the wall. The turbulent viscosity ν_t is modeled based on mixing length theory with near-wall damping.

$$\frac{1}{\mathrm{Re}_t} = \frac{\kappa}{\mathrm{Re}} d^+ \left(1 - e^{-d^+/A}\right)^2 \tag{11}$$

Where, κ is Von-Karman constant, d is normal distance from the wall, A= 19 and,

$$d^+ = \frac{u_\tau d}{\nu} \tag{12}$$

$$u_\tau = \sqrt{\frac{\tau_w}{\rho}} \tag{13}$$

$$\|\tau_w\| = \left(\frac{1}{\mathrm{Re}} + \frac{1}{\mathrm{Re}_t}\right) \frac{\partial u_t}{\partial n} \Big|_{wall} \tag{14}$$

Equation (10) is discretized using the second order central difference scheme and solved using an efficient tri-diagonal solver. Equation (14) is then used to obtain the wall shear stress in the tangential direction, the components of which are then transformed back into a (*x,y,z*) coordinate system to act as boundary conditions in the respective momentum equations for the outer flow completing the coupling with the outer flow.

2.3 Zonal two layer heat transfer model

The energy equation for turbulent flows in conservative non-dimensional form for a coordinate system of reduced dimensionality (*t,n)* can be written as

$$\frac{\partial \theta}{\partial T} + \frac{\partial (u_n \theta)}{\partial n} + \frac{\partial (u_t \theta)}{\partial t} = \frac{\partial}{\partial n}\left[\left(\frac{1}{\mathrm{Re} \cdot \mathrm{Pr}} + \frac{1}{\mathrm{Re}_t \cdot \mathrm{Pr}_t}\right)\frac{\partial \theta}{\partial n}\right] + S_\theta \tag{15}$$

In absence of additional source terms and negligible advection, it can be simplified to,

$$\frac{\partial}{\partial n}\left[\left(1 + \frac{\mathrm{Re} \cdot \mathrm{Pr}}{\mathrm{Re}_t \cdot \mathrm{Pr}_t}\right)\frac{\partial \theta}{\partial n}\right] = 0 \tag{16}$$

The solution of Equation (16) requires the closure model for the turbulent Prandtl number. For the current investigation, the formulation of Kays [40] is used and presented in Equation (17).

$$1/\mathrm{Pr}_t = 0.58 + 0.22\left(\frac{\mathrm{Re}}{\mathrm{Re}_t}\right) - 0.0441\left(\frac{\mathrm{Re}}{\mathrm{Re}_t}\right)^2 \left\{1 - \exp\left[\frac{-5.165}{\left(\frac{\mathrm{Re}}{\mathrm{Re}_t}\right)}\right]\right\} \tag{17}$$

This formulation accounts for the higher values of turbulent Prandtl number very close to the wall and its gradual decay away from the wall. Equation (16) is solved in the inner layer zonal mesh in a same way as Equation (10). The temperature at the first LES grid point off the wall and either the specified wall temperature or the surface heat flux are used as boundary conditions for solving Equation (16). If the heat flux at the wall is specified, then there is no change in the energy equation calculation for the outer layer. Still, Equation (16) is solved in the inner layer to obtain the wall temperature using the outer LES temperature and specified wall heat flux as a boundary condition. The temperature profile obtained from solving Equation (16) in the inner layer is used to calculate the wall temperature as follows

$$\theta_{wall} = \theta_{i2} + \frac{\Delta d}{\left(1 + \frac{\mathrm{Re\,Pr}}{\mathrm{Re}_t\,\mathrm{Pr}_t}\right)} \tag{18}$$

where, θ_{i_2} is the temperature at the first off wall inner layer nodal point and Δd is its normal distance from the wall.

2.4 Synthetic eddy method formulation

The synthetic eddy method uses randomly distributed eddies in an eddy container around the inlet plane with a velocity shape function associated with each eddy. The eddies behave much like real eddies in that they convect in the eddy container based on the mean velocity of the flow. Inlet turbulence is generated by taking the collective effect of all the eddies on the velocity nodes in the inlet plane, conditioned by the available turbulent statistics. The net result is the generation of instantaneous turbulence, which is spatially and temporally correlated based on the measured integral length scales and the mean velocity profile input into the method.

A container for vortical structure is formed around the inlet plane using the known length scales $l_{i,j}$ of each velocity component i, in each direction j with bounds defined by following two equations.

$$\begin{aligned} x_j^+ &= x_j + \max\left(l_{ij}\right) \\ x_j^- &= x_j - \min\left(l_{ij}\right) \end{aligned} \tag{19}$$

The instantaneous velocity signal at each nodal point is expressed as a cumulative effect of local velocity fluctuations from each eddy around it.

$$u_i\left(x_j,t\right)=U_i\left(x_j\right)+\sqrt{\frac{1}{N}\sum_{S=1}^{N}\varepsilon_i^S f_{l_{i,j}} dx_i^S} \qquad (20)$$

The shape function f here is represented as

$$f_{l_{i,j}} dx_i^S = \sqrt{vol_c}\,\frac{1}{l_{i1}} f\left(\frac{x_1-x_1^S}{l_{i1}}\right)\frac{1}{l_{i2}} f\left(\frac{x_2-x_2^S}{l_{i2}}\right)\frac{1}{l_{i3}} f\left(\frac{x_3-x_3^S}{l_{i3}}\right) \qquad (21)$$

Where Vol_c is the total volume of the container of the eddies. N is the number of eddies and ε_i^S are the intensities of each eddy. x_i^s represent the position of each coherent structure (eddy). Initial placement of the coherent structures is taken from a uniform distribution over the container volume. Intensities of the coherent structures are given as

$$\varepsilon_i^S = r_{ij} c_j^S \qquad (22)$$

Where $r_{ij}$is the Cholesky decomposition of Reynolds stress tensor R_{ij} and $c_j^S$are independent random variables taken from a distribution with zero mean and variance of unity. In current study, the shape function f, which characterizes the decay of perturbations created by each coherent structure around its center is represented as

$$\begin{aligned} f_l\left(r\right) &= \sqrt{\frac{3}{2l}\left(1-\left|\frac{r}{l}\right|\right)} && \text{if } \left|r\right|<1 \\ f_l\left(r\right) &= 0 && \text{otherwise} \end{aligned} \qquad (23)$$

The eddies are convected through the inflow plane with the bulk mean velocity U_b over inlet plane P to ensure that the synthetically generated signal is accurate in time.

$$x_i^S\left(t+dt\right)=x_i^S\left(t\right)+U_{b,i}dt \qquad (24)$$

Once the coherent structure is convected outside the container, it is regenerated upstream and its intensities are calculated again. This signal has spatial and temporal correlations and satisfies $\left\langle u_i^{'}\right\rangle=0$ and $\left\langle u_i^{'}u_i^{'}\right\rangle=\delta_{ij}$.

2.5 Numerical method

The governing equations for momentum and energy are discretized with a conservative finite-volume formulation using a second-order central difference scheme on a non-staggered grid topology. The Cartesian velocities, pressure, and temperature are calculated and stored at the cell center, whereas contravariant fluxes are stored and calculated at cell faces. For the time integration of the discretized continuity and momentum equations, a projection method is used. The temporal advancement is performed in two steps, a predictor step, which calculates an intermediate velocity field, and a corrector step, which calculates the updated velocity at the new time step by satisfying discrete continuity. The energy equation is advanced in time by the predictor step. In all the simulations 64 virtual grid points are used in inner layer. This number is based on the y^+ values of the first off wall LES node and previous studies performed by Patil and Tafti [41]. The computer program Generalized Incompressible Direct and Large Eddy Simulations of Turbulence (GenIDLEST) used for current study has been applied and validated for numerous complex heat transfer and fluid flow problems. Details about the algorithm, functionality, and capabilities can be found in Tafti [42, 43].

All calculations were performed on 39 Apple Xserve G5 compute nodes with 2.3 GHz PowerPC 970FX processor. All WMLES calculations performed at Re=50,000 and 80,000 used a non-dimensional time step of 1×10^{-4}. For integrating over one non-dimensional time unit, about 38 hours of wall clock time is utilized. Calculations are initiated assuming initial bulk velocity and integrated in time till statistically stationary conditions are reached. The time evolution of various bulk quantities like skin friction, Nusselt number are monitored to ascertain the flow has reached statistically stationary state. Once stationary conditions are established, data sampling is initiated to obtain mean and turbulent quantities. Sampling interval is 5 non-dimensional time units for all calculations. Initial mean quantities of velocities are obtained by sampling over 1 time unit before beginning to sample fluctuating quantities for turbulent statistics.

3 RESULTS

3.1 Computational domain

Figure 2 shows the sketch of the experimental and computational geometry. Two computational domains are identified – one which was used by Patil et al. [1] for RANS calculations (red box), which included the swirler in the computational geometry, and the other shorter domain (blue box), which is used in the current LES simulations. The details of the RANS simulations can be found in Patil et al. [1]. In order to reduce the computational complexity and cost, the LES domain is selected in the region of interest, which includes the can combustor and a section 0.5H upstream of it as shown in Figure 2. At the inlet plane of the LES domain, data is extracted from RANS solution and interpolated onto the LES grid and used for synthetically generating the inlet turbulence.

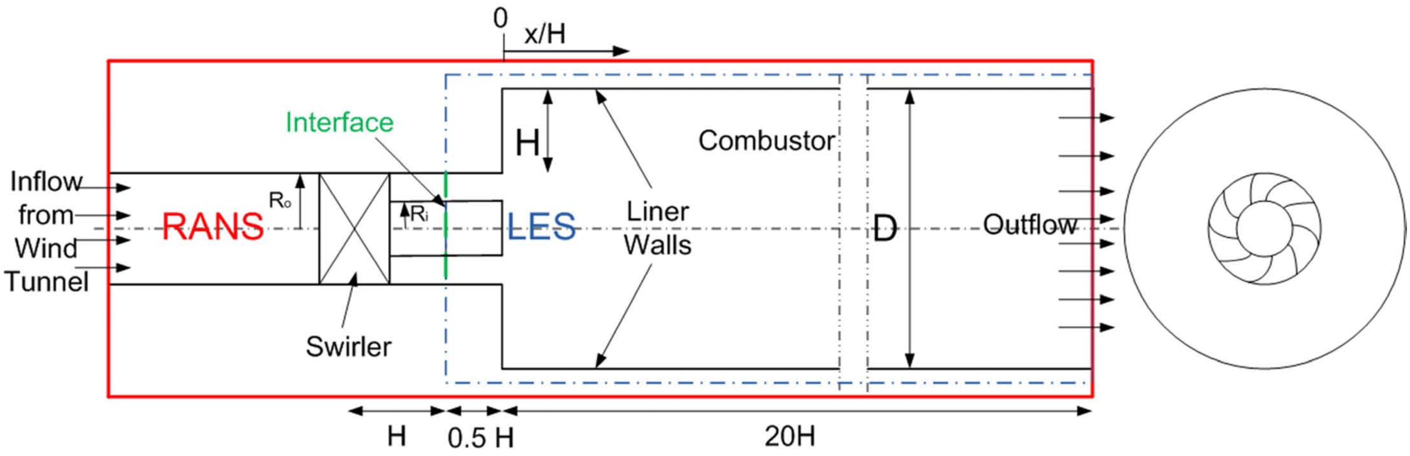

Figure 2: Schematics of experimental setup of Patil et al. [1] (From left to right: swirler, nozzle extension channel, and can combustor. RANS domain is shown in red. LES domain is shown in blue and the interface between RANS and LES is shown by green line.) ($L^*=D=203$ mm, $H=0.3D$) (Swirl nozzle details: $R_i=0.11D$, $R_o= 0.2D$)

Figure 3 shows the frontal and side view of a three dimensional mesh inside the LES computational domain. A block structured mesh with hexahedral cells is formed using GRIDGEN software tool.

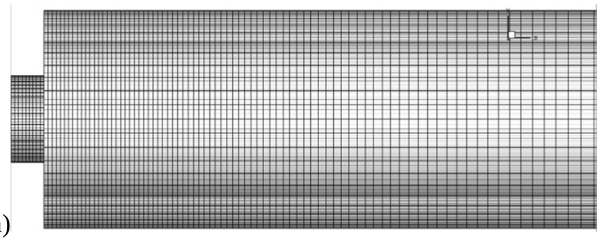

(a)

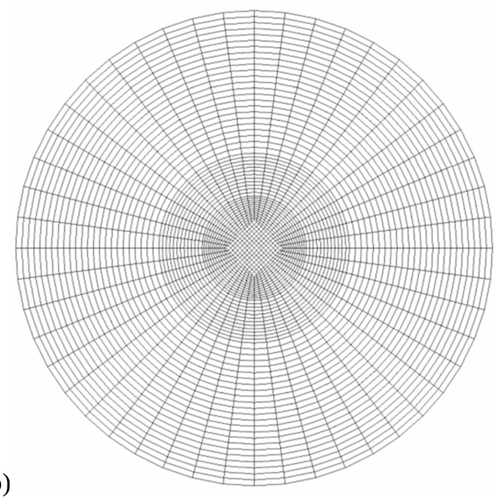

(b)

Figure 3: 3D computational domain (a) frontal view of the mesh (b) side view of the mesh

Two different Reynolds numbers, 50,000 and 80,000 are investigated. The Reynolds number is based on the diameter of the can combustor (D) and bulk mean velocity inside it (U_b). The Swirl number defined as the ratio of the axial flux of circumferential momentum to the axial flux of axial momentum times the reference inflow section radius is represented by Equation (25).

$$S = \frac{\int_{R_i}^{R_o} U U_\theta r^2 dr}{R_o \int_{R_i}^{R_o} U^2 r dr} \qquad (25)$$

In Equation (25), U and U_θ are the mean axial and tangential velocity, respectively. R_i and R_o are outer and inner radii of the swirl nozzle. The characteristic Swirl number defined by Equation (25) is fixed at value of 0.7 at the inlet of the LES domain for the simulations performed. The computational mesh for all simulations consists of $240 \times 138 \times 160$ grid points in the axial, radial, and circumferential directions, respectively. The values of Y^+ on the combustor liner wall were observed to be in the range of 30-60 for the calculations performed. A convective outflow boundary condition is used at the exit of the can combustor, which is 20 step heights downstream of the expansion into the can combustor. All the walls were treated as no-slip boundaries. A constant heat flux thermal boundary condition is specified at the combustor liner wall while all other walls are treated as adiabatic with zero heat flux.

3.2 Inlet flow profiles

Three components of mean velocity and Reynolds stresses are extracted from the RANS solution of Patil et al. [1]. Reduced data is available from the RANS data of Patil et al. [1]

in the form of mean velocity, turbulent kinetic energy and its dissipation rate. Figure 4 shows the profiles of the three velocity components, normalized by the bulk mean combustor velocity and turbulent kinetic energy, normalized by the square of the bulk mean combustor velocity. Reynolds normal stresses are extracted from the RANS solution using the following Equation (26)

$$R_{ii} = \overline{u_i'^2} = \frac{2}{3}k \tag{26}$$

where i=1,2,3. The length scales of coherent structures at the inlet plane are found using Equation (27).

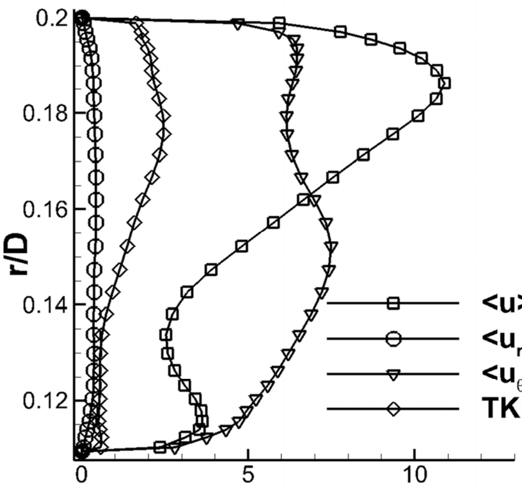

Figure 4: Profiles of mean velocity (normalized by bulk mean velocity in combustor) and turbulent kinetic energy (normalized by square of bulk mean velocity in combustor) at the inlet plane of the LES computational domain (x/H=-0.5) (Re=50,000, Swirl number = 0.7)

$$l = c_\mu \frac{k^{3/2}}{\varepsilon} \tag{27}$$

where k is the turbulent kinetic energy and ε is the dissipation rate of the turbulent kinetic energy and value of constant $c_\mu = 0.0845$. The near wall length scale was limited by the local grid size of the LES, as length scale calculation based on the Equation (27) might go to zero at the near wall cell. This limiting criterion also guarantees that the synthetic coherent structures can be discretized by the LES grid.

3.3 Validation of computational methodology

A detailed validation of the computational methodology described in Section 2 has been carried out by Patil and Tafti [44] in comparison to the measurements of Wang et al. [7] in a can combustor configuration. Computations were carried out at a Reynolds number of 20,000 (based on inflow bulk velocity and diameter) and the characteristic Swirl number of 0.43. The synthetic eddy method was used to generate turbulence at the inlet plane of the computational domain (x/H=-2.1) using experimental LDV data [7]. Wall resolved LES was carried on a very fine grid (5 million cells), while the two layer wall model was applied on a relatively coarse mesh (1.5 million). Comparison between the wall resolved, wall modeled LES calculations and the LDV data was carried out at 12 different axial locations in the range of x/H=-2.1 to x/H=10. While these comparisons were in very good agreement at all stations, for brevity only 3 locations, x/H=0.17, x/H=2.1, and 6.3 are shown in Figure 5.

The first location in Figure 5 is immediately downstream of the sudden expansion, the second in the vortex breakdown region, and the last in the region where swirl starts decaying. Both wall resolved and wall modeled LES predictions are in good agreement with the experimental data. LES is able to accurately predict the steep gradients in the swirl velocity in the shear layer as observed in the experiments. Accurate predictions by the wall modeled LES shows that the two layer wall model also provides a good estimate of the wall shear stress.

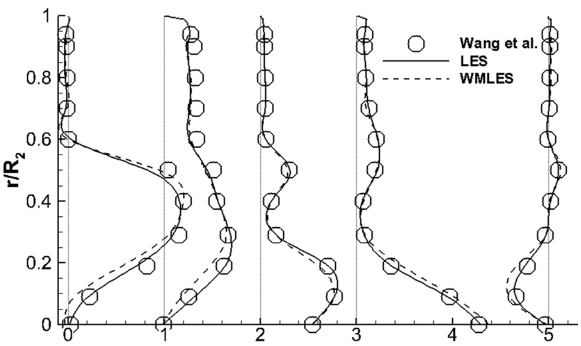

a)

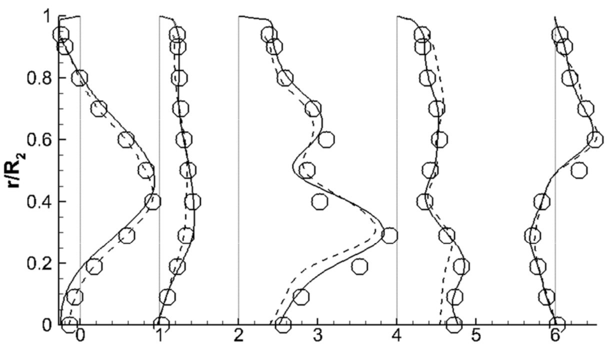

(b)

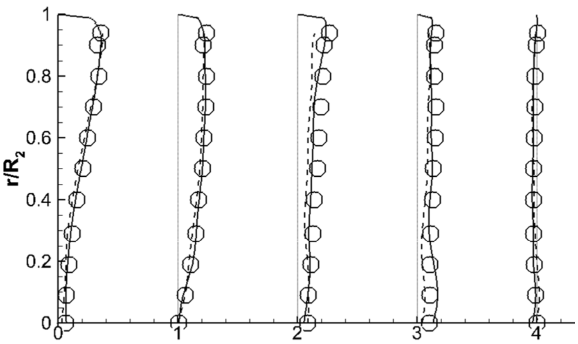

(c)

Figure 5: Time averaged profiles of (from left to right) axial velocity ($<u>/U_b$)(scale 1:1), swirl velocity($<u_\theta>/U_b$)(scale 1:1), variance of axial velocity ($<u'u'>/U_b^2$)(scale 1:8), variance of swirl velocity ($<u'_\theta u'_\theta>/U_b^2$)(scale 1:8), Reynolds shear stress ($<u'u'_r>/U_b^2$)(scale 1:10) for Re=20,000 and S=0.43 at (a) $\frac{x}{H} = 0.17$, (b) $\frac{x}{H} = 2.1$, and (c) $\frac{x}{H} = 6.3$
(R_2 is the combustor radius, R_2=L*)

Figure 5 also shows that both wall resolved and wall modeled LES capture the anisotropic turbulent structure with good accuracy within experimental uncertainty. The higher magnitudes of variances of streamwise and circumferential velocity at the beginning of the combustor section, which are characteristic of swirling flows, are captured well in the computations. Also, the fast decay of turbulence downstream of the vortex breakdown region is captured accurately. These results give us confidence that the synthetic eddy method used in conjunction with wall layer modeling can accurately predict the flow in a can combustor.

Comparing the spatial resolution for wall resolved LES and computational time step, wall modeled LES reduces the computational complexity by a factor of 9.

3.4 Reynolds number 50,000

3.4.1 Flow-field characteristics

A detailed flow-field analysis is carried out to study various characteristics of the swirl dominated flow inside the combustor and its interaction with the liner wall. Figure 6 (a) represent the mean streamline pattern (only averaged for 2 non-dimensional time units) in the combustor in an azimuthal plane (z=0). Figure 6(a) expresses many important mean flow features of the swirl dominated field in the combustor. Flow separates at the lower edge of the step expansion resulting in a corner recirculation bubble near the upper edge of the step expansion.

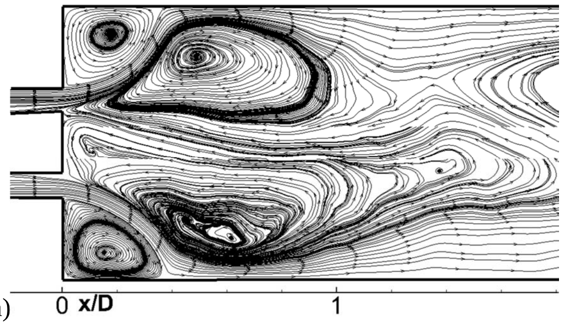

(a)

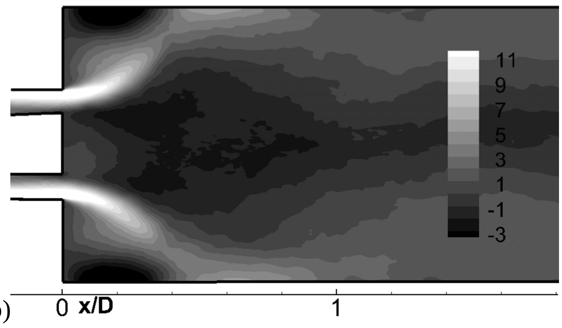

(b)

Figure 6: (a) Mean flow streamlines in the azimuthal plane (z=0) (b) Contours of axial velocity (normalized by bulk mean combustor velocity) in azimuthal plane (z=0)
(Re = 50,000)

A vortex breakdown process occurs immediately after the step expansion resulting in a swirl induced internal recirculation region. Presence of this central recirculation region is one of the important characteristic features of the highly turbulent swirling flow. The flow reattaches around a step height after the separation. This reattachment length is much shorter than the one observed in non-swirling flows (typical value of reattachment length for non-swirling flows is around 6 step heights). Higher swirl strength results in higher spread angle of the shear layer coming out of the swirl nozzle and expanding into the combustor.

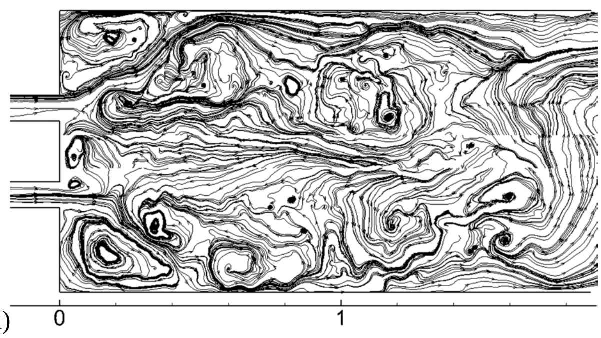

(a)

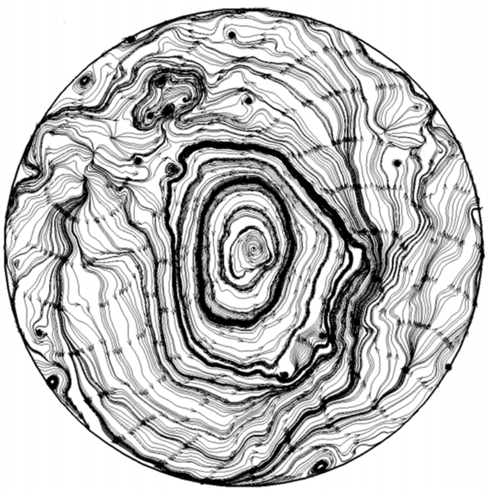

(b)

Figure 7: Streamlines in an instantaneous flowfield at (a) azimuthal plane (z=0) and (b) Streamwise location x/D=0.5 (Re = 50,000)

An instantaneous streamline pattern is shown in Figure 7. From Figure 7(a), it is evident that the region downstream of expansion is dominated by the vortex breakdown process. The streamlines in this region show a flow reversal resulting in an internal recirculation zone. Figure 7(b) represents strong swirling flow in the upstream region of combustor at streamwise location x/D=0.5. Streamlines pattern is not smooth in this cross section, representing the presence of several smaller coherent structures.

Figure 6(b) represent the distribution of the axial velocity normalized by the bulk mean combustor velocity in the azimuthal plane (z=0). Figure 6(b) helps in visualizing the energetic shear layer coming out of the swirl nozzle, expanding into the combustor and impinging on the liner wall. High negative velocities are observed near the upper edge of the expansion representing the presence of the corner recirculation zone. Similarly, the central recirculation zone is also characterized by the presence of negative velocities.

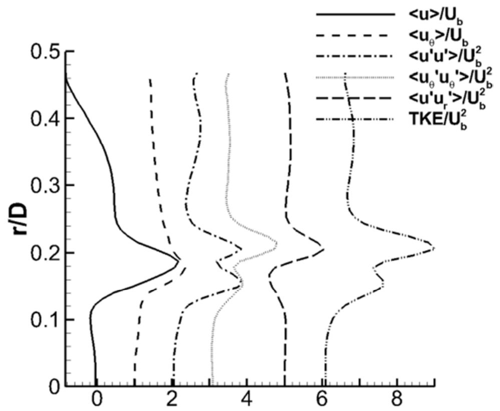

(a)

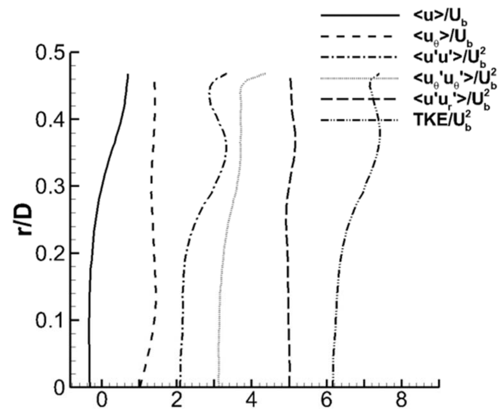

(b)

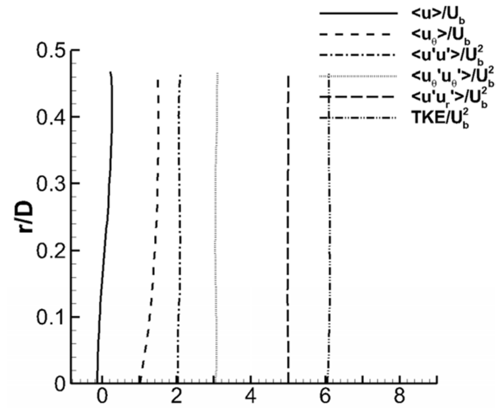

(c)

Figure 8: Variation of mean velocity components and Reynolds stresses at (a)x/D=0.1 (b)x/D=0.45 (c)x/D=2 (scale 6:1) (Re=50,000)
(All quantities are circumferentially averaged and plotted along the radial direction. Mean velocities are normalized by the bulk mean combustor velocity while the Reynolds stresses are normalized by the square of the bulk mean combustor velocity.)
(Graphs are obtained by plotting the normalized values around the vertical lines at x axis values of 0,1,2,3,5, and 6)

To further quantify and analyze the flow-field in the combustor, variation of all three components of the velocity and Reynolds stresses averaged in the circumferential direction was studied throughout the combustor at several axial locations. Figure 8 represents the variation of mean axial and swirl velocity, variances of axial velocity and swirl velocity, Reynolds shear stress and turbulent kinetic energy along the radial direction at three representative streamwise locations. These locations are chosen as immediately after the expansion (x/D=0.1), near the impingement location(x/D=0.4), and further downstream in the region (x/D=2) of decaying turbulent swirling flow.

Figure 8(a) represents the mean velocity and Reynolds stresses immediately after the step expansion. Mean axial as well as circumferential velocity show significantly higher values in the range of r/D of 0.15 to 0.22 expressing the presence of the shear layer. The mean axial velocity reaches significantly high negative values in the corner circulation bubble near the combustor liner (r/D=0.5). It also has slight negative values in the region of r/D=0 to r/D=0.15, which represents the swirl induced recirculation bubble shown in Figure 6(a). The variances of all three velocity components differ considerable from each other. This was observed to a greater extent at least four step heights after the expansion. This indicates high turbulence anisotropy in the flowfield. The values of variances of swirl velocity and radial velocity were observed to be significantly high near the step expansion. This is another differentiating feature between swirling and non-swirling flows. This also reflects in the significantly higher values of turbulent kinetic energy seen in Figure 8.

Figure 8(b) represent that the axial velocity has very high magnitude near the region of shear layer impingement at the liner wall. The value of swirl velocity is also significantly higher at this location. It is also important to note that the variances of axial and swirl velocity are very high in this region. The turbulent kinetic energy shown in Figure 8(b) exhibits a very high value near r/D=0.5.

After the flow impingement location, the turbulent swirling flow was observed to decay at a very fast rate. Figure 8(c) represents the mean velocity and Reynolds stresses further downstream. The peak values of axial and swirl velocity are reduced significantly at this location. More importantly, the variances of the mean velocity and swirl velocity have significantly lower values. This indicates the faster decay of turbulent swirling flow. This observation is consistent with previous observations in the literature [1, 3, 5-7].

3.4.2 Liner wall heat transfer

Figure 9 compares the predictions from LES calculation for Reynolds number of 50,000 with the experimental data of Patil et al. [1]. The heat transfer coefficient at the liner wall is characterized by the Nusselt number augmentation ratio, where the baseline Nusselt number is obtained from the Dittus-Boelter correlation for fully-developed pipe flow with heated walls as expressed in Equation (28).

$$Nu_0 = 0.023 \times \mathrm{Re}^{0.8}\,\mathrm{Pr}^{0.4} \tag{28}$$

where Pr is Prandtl number with value of 0.7 in all the calculations performed. The local Nusselt number is calculated as

$$Nu = \frac{1}{\theta_w - \theta_{in}} \tag{29}$$

where θ_w is the local liner wall surface temperature, and θ_{in} is the inlet temperature.

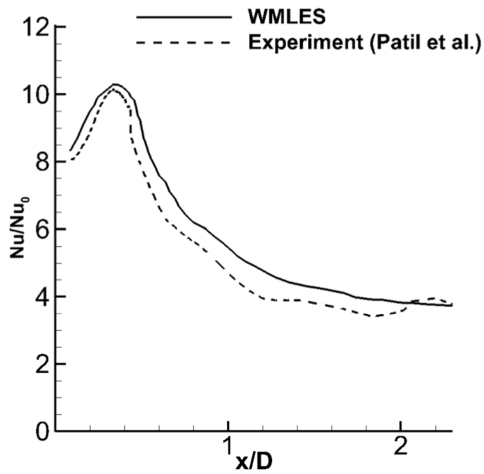

Figure 9: Heat transfer augmentation ratio (Nu/Nu_0) along the liner wall (Re=50,000)

Circumferentially averaged values of Nusselt augmentation are plotted versus the axial distance normalized by the diameter of the can combustor. It can be observed from Figure 10 that the prediction of the heat transfer coefficient is in good agreement with the experimental data. The heat transfer augmentation increases from the beginning of the combustor (immediately after step expansion), reaches a maximum value and then decays at fast rate. WMLES predictions follow the trend of heat transfer coefficient measured by the experiment. More importantly, the value of peak heat transfer augmentation predicted by the WMLES is in very close agreement with the experiment. It is also important to note that the location of peak heat transfer predicted by WMLES is in exact agreement with the experimental findings and occurs in the region of shear layer impingement, which results in large velocity gradients at the liner wall and high turbulent intensities. The close agreement between experiments and predictions validate all the major components used in the simulations, i.e., accurate reconstruction of instantaneous velocities at the inlet to the computational domain by the SEM using data from a precursor RANS simulation and accurate modeling of the inner layer velocity and temperature field by the wall model.

3.5 Reynolds number 80,000

3.5.1 Flow-field characteristics

Figure 10(a) represents the mean flow streamlines for Reynolds number of 80,000 in azimuthal plane (z=0) (only averaged for two non-dimensional time units). The streamline pattern is very similar to the one observed for Reynolds number of 50,000. Major flow features exhibit similar behavior for both the Reynolds numbers. A vortex breakdown process occurs immediately downstream of the step expansion resulting in an internal recirculation region. The extent of this internal recirculation region is the same as for the low Reynolds number

(Re=50,000). More importantly, the size of the corner recirculation zone remains exactly the same for this higher Reynolds number. The spread angle of the highly energetic shear layer issuing from the swirl nozzle is also the same for both the Reynolds numbers. This results in the impingement location of the shear layer on the liner wall to be exactly the same for both Reynolds numbers. Figure 10(b) represent the contours of the time averaged mean axial velocity normalized by the bulk mean combustor velocity in the azimuthal plane (z=0). The distribution of the normalized axial velocity also behaves the same as for Reynolds number of 50,000. These flow features point out that for the Reynolds number range investigated, the major flow features in the combustor are held fixed by the Swirl number, which is constant at a value of 0.7.

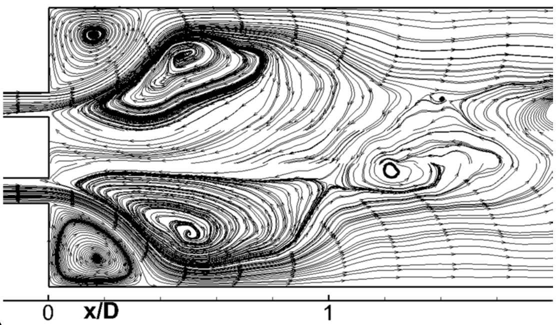

(a)

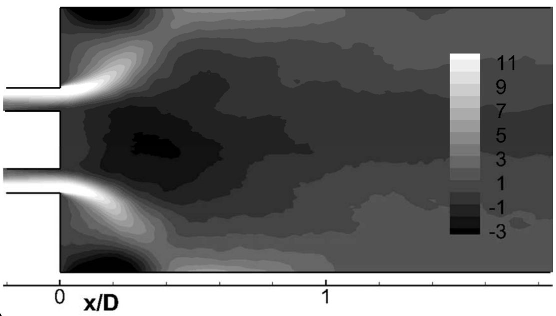

(b)

Figure 10: (a) Mean flow streamlines in the azimuthal plane (z=0) (b) Contours of axial velocity (normalized by bulk mean combustor velocity) in azimuthal plane (z=0)(Re = 80,000)

This observation is consistent with the findings of Patil et al. [1] who noted that even an order of magnitude further increase in Reynolds number does not change the location of shear layer impingement.

Figure 11 represent the variation of mean velocity components and Reynolds stresses at three representative streamwise locations. Mean velocity components were normalized by the bulk mean combustor velocity while the Reynolds stresses are normalized by the square of bulk mean combustor velocity. These quantities are circumferentially averaged and plotted against the radial co-ordinate normalized by the combustor diameter. The variation of mean velocity and their variances follows trends similar to that observed for a Reynolds number of 50,000. This is consistent with the observation previously made that the major flow structures are not dependent on the Reynolds number. The values of normalized Reynolds stresses are nearly the same as for the lower Reynolds number. This indicates that even though the turbulence production increases with Reynolds number, the normalized values of Reynolds stresses do not increase. The values of turbulent intensities are high near the impingement location, which leads to the peak in heat transfer.

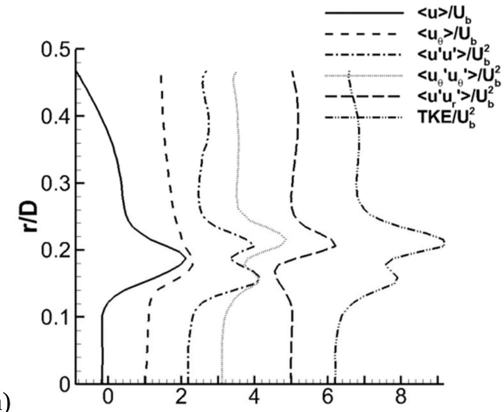

(a)

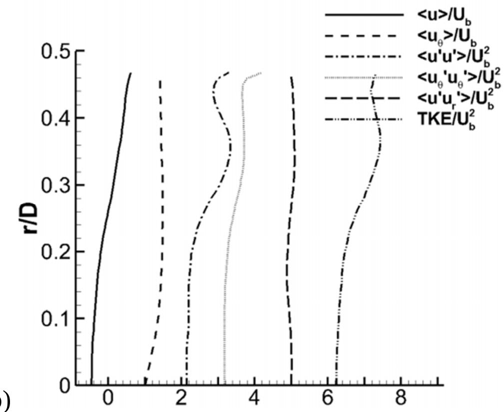

(b)

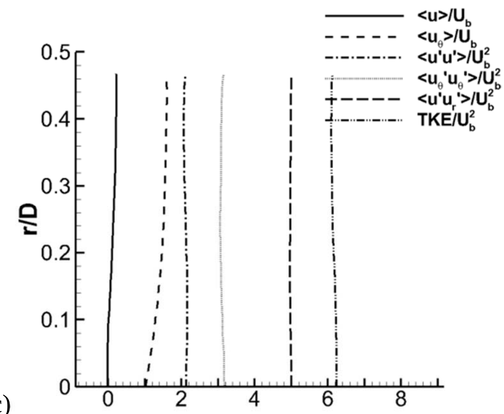

(c)

Figure 11: Variation of mean velocity components and Reynolds stresses at (a)x/D=0.1 (b)x/D=0.45 (c)x/D=2 (scale 6:1) (Re=80,000)

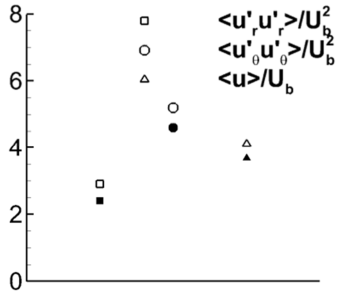

Figure 12: Normalized Reynolds normal stresses and axial velocity in the shear layer near the peak heat transfer location (Empty symbols are fore Re=50,000 and filled symbols are for Re=80,000. Axial location = (x/D=0.45). Radial location = (r/D=0.45)

Figure 12 represent the normalized Reynolds normal stresses and axial velocity near the peak location. It is observed that the values of the peak heat transfer location are little lower for Reynolds number of 80,000. The turbulence production in the shear layer is dependent on the Reynolds number as well as the swirl strength. However, with the increase in Reynolds number the Swirl number remains constant at 0.7 since it is largely dependent on the injector vane geometry. Hence, although turbulent production increases in the impinging shear layer as a result of increased Reynolds number, the normalized value decreases because it is strongly dependent on the Swirl number, which remains the same. It is also noted that reduction in normalized turbulence intensities is also associated with the slightly lower magnitudes of normalized axial velocity.

The turbulent swirling flow starts decaying at a fast rate after the impingement location. From Figure 11(c), we can observe that the values of turbulence intensities are very low representing the decayed turbulent swirl flow.

3.5.2 Liner wall heat transfer

Figure 13 shows the distribution of Nusselt number augmentation on the combustor liner wall. The heat transfer coefficient distribution correlates with the flow patterns observed. The trends in Nusselt augmentation are similar to Reynolds number 50,000 case. WMLES is able to predict the trends and magnitudes of heat transfer coefficient in close agreement with the experimental data. It is important to note that peak Nusselt augmentation has reduced from a value 10.2 to 8. As observed in the flow-field analysis, the normalized turbulence intensities in the wall normal and azimuthal direction are lower for Reynolds number of 80,000. This is also associated with the lower normalized axial velocity in the shear layer near the peak location. These are the major reasons for the drop in peak heat transfer augmentation.

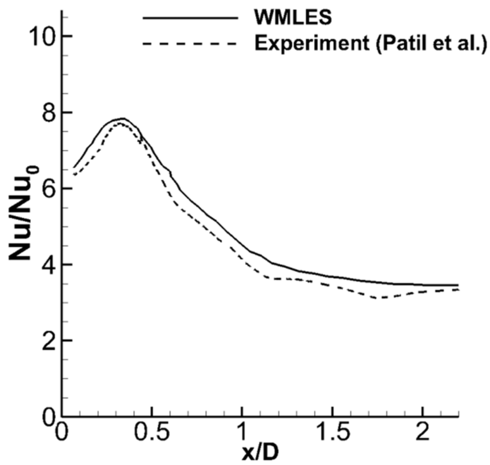

Figure 13: Heat transfer augmentation ratio (Nu/Nu_0) along the liner wall (Re=80,000)

The location of peak heat transfer on the other hand remains the same for both Reynolds number. This can be correlated with the observation made in the flow-field analyses that the size of the corner recirculation zone, shear layer spread angle and flow impingement location on the liner wall remains same for both Reynolds number. This is because for the Reynolds number range investigated, the same Swirl number holds the flow features in the combustor constant. Good agreement of the heat transfer coefficient value on the combustor liner wall with the experiments shows that the near wall treatment both for velocity and temperature presented in Section 2 is able to accurately represent the region close to wall in complex flows at high Reynolds numbers.

4 CONCLUSIONS

Large-eddy simulations are performed to investigate the flow and the associated convective heat transfer in a gas turbine can combustor under cold flow condition. The computational model is built with two major interests. First, to evaluate the ability of the formulated synthetic eddy method to represent the inlet turbulence in hybrid RANS-LES calculations in complex gas turbine configurations; second, to test the accuracy of the integrated velocity-thermal zonal near wall treatment of turbulence in a generalized co-ordinate system LES framework to reduce the total computational time. To achieve these objectives, LES calculations were performed with inlet turbulence simulated synthetically using inflow data from a precursor RANS simulation and near wall region represented by a zonal two layer model. Two high Reynolds numbers of 50,000 and 80,000 were investigated with a characteristic Swirl number of 0.7.

It is observed that the flow-field in the combustor is characterized by a highly energetic shear layer, a swirl induced central recirculation zone, corner recirculation zones and fast decay of swirl and turbulence, downstream of the impingement. An impinging shear layer, resulting in a steep velocity gradient and high turbulent intensities, is responsible for very high values of heat transfer augmentation at the peak location. It is observed that at higher Reynolds number the values of normalized turbulence intensities in wall normal and spanwise direction are lower. This, together with a lower normalized axial velocity in the shear layer near the peak location causes a drop in Nusselt augmentation with increase in Reynolds number. The major flow structures are held constant by a fixed Swirl number for both Reynolds numbers. This results in very similar flow structure in the combustor with no change in the peak heat transfer location.

WMLES predictions are able to simulate the anisotropic flowfield inside the combustor and are able to capture the trends and values of the heat transfer coefficient in close agreement with the experimental data. Importantly, the magnitude and location of peak heat transfer is predicted in very close agreement with the experiment. The close agreement between experiments and predictions validate all the major components used in the simulations, i.e., accurate reconstruction of instantaneous velocities at the inlet to the computational domain by the SEM using data from a precursor RANS simulation, and accurate modeling the of inner layer velocity and temperature field by the wall model.

ACKNOWLEDGMENTS

The calculations were performed on Virginia Tech's Terascale computing facility, System-X. The support is gratefully acknowledged. We also acknowledge the support provided by Solar Turbines in gas turbine combustor liner heat transfer, which motivated the authors in doing this study.

REFERENCES

[1] Patil S., Abraham S., Tafti D., Ekkad S., Kim Y., Dutta P., Moon H., and Srinivasan R., 2011. "Experimental and numerical investigation of convective heat transfer in gas turbine can combustor," Journal of Turbomachinery, **133(1)**, 011028-1-7.

[2] Starkey P. A., and Yim M. J., 2007. "Experimental and numerical investigation of a swirl stabilized premixed combustor under cold-flow conditions," Journal of Fluids Engineering, **129**, 942-953.

[3] Nejad A. S., Vanka S. P., and Favaloro S. C., 1989. "Application of laser velocimetry for characterization of confined swirling flow," Journal of Engineering Gas Turbines Power, **111(1)**, 36-45.

[4] Weber R., Visser B., and Boysan F., 1990. "Assessment of turbulence modeling for engineering prediction of swirling vortices in the near burner zone," International Journal of Heat and Fluid Flow, **11(3)**, 225-235.

[5] Kitoh O., 1991. "Experimental study of turbulent swirling flow in a straight pipe," Journal of Fluid Mechanics, **225**, 445-479.

[6] Ahmed S. A., 1998. "Velocity measurements and turbulence statistics of a confined isothermal swirling flow," Experimental Thermal Fluid Sciences, **17**, 256-264.

[7] Wang P., Bai X., Wessman M., and Klingmann J., 2004. "Large eddy simulation and experimental studies of a confined turbulent swirling flow," Physics of Fluids, **16(9)**, 3306-3324.

[8] Patil S., Sedalor T., Tafti D., Ekkad S., Kim Y., Dutta P., Moon H., and Srinivasan R., 2011. "Study of flow and convective heat transfer in a simulated scaled up low emission annular combustor," Thermal Science and Engineering Application, submitted.

[9] Grinstein F., and Fureby C., 2005. "LES studies of the flow in a swirl gas turbine combustor," Proceedings of Combustion Institute, **30**, 1791-1798.

[10] Wang S., Yang V., Hsiao G., Hsieh S., and Mongia H., 2007. "Large-eddy simulation of gas-turbine swirl injector flow dynamics," Journal of Fluid Mechanics, **583**, 99-122.

[11] Pierce C. D., and Moin P., 1998. "Large eddy simulation of a confined coaxial jet with swirl and heat release," AIAA 98-2892, 29th AIAA Fluid Dynamics Conference, 15–18 June 1998.

[12] Kim W. W., Menon S., and Mongia H. C., 1999. "Large-eddy simulation of a gas turbine combustor flow," Combustion Science and Technology, **143**, 25-62.

[13] Chapman D. R., 1979. "Computational aerodynamics, development and outlook," AIAA Journal, **17**, 1293–313.

[14] Deardorff J. W., 1970. "A numerical study of three-dimensional turbulent channel flow at large Reynolds numbers," Journal of Fluid Mechanics, **41**, 453–480.

[15] Schumann U., 1975. "Subgrid-scale model for finite difference simulation of turbulent flows in plane channels and annuli," Journal of Computational Physics, **18**, 376–404.

[16] Grotzbach G., 1987. "Direct numerical and large eddy simulation of turbulent channel flows," In Encyclopedia of Fluid Mechanics, ed. NP Cheremisinoff, 1337–91. West Orange, NJ: Gulf Publication.

[17] Werner H., and Wengle H., 1993. "Large-eddy simulation of turbulent flow around a cube in a plane channel," In Selected Papers from the 8th Symposium on Turbulent Shear Flows.

[18] Piomelli U., Moin P., Ferziger J., and Kim J., 1989. "New approximate boundary conditions for large-eddy simulations of wall-bounded flows", Physics of Fluids A, **101**, 61–68.

[19] Hoffmann G., and Benocci C., 1995. "Approximate wall boundary conditions for large-eddy simulations," In: Benzi, R. (Ed.), Advance in Turbulence V, 222–228.

[20] Temmerman L., Leschziner M. A., and Hanjalic K., 2002. "A-priori studies of a near-wall RANS model within a hybrid LES/RANS scheme," In: Rodi, W., Fueyo, N. (Eds.), Engineering Turbulence Modeling and Experiments, Elsevier, 317–326.

[21] Spalart P. R., Jou W. H., Strelets M., and Allmaras S. R., 1997. "Comments on the feasibility of LES for wings and

on a hybrid RANS/LES approach," Advances in DNS/LES, 137–48, Columbus, OH.

[22] Nikitin N. V., Nicoud F., Wasistho B., Squires K. D., and Spalart P. R., 2000. "An approach to wall modeling in large-eddy simulations," Physics of Fluids Letters, **12**, 1629-1632.

[23] Viswanathan A. K., and Tafti D. K., 2006. "Detached eddy simulation of turbulent flow and heat transfer in a two-pass internal cooling duct," International Journal of Heat and Fluid Flow, **27(1)**, 1-20.

[24] Balaras E., and Benocci C., 1994. "Subgrid-scale models in finite-difference simulations of complex wall bounded flows," AGARD CP 551, 2.1–2.5, Neuilly-Sur-Seine, France: AGARD.

[25] Balaras E., Benocci C., and Piomelli U., 1996. "Two layer approximate boundary conditions for large-eddy simulations," AIAA Journal, **34**, 1111–1119.

[26] Cabot W., and Moin P., 1999. "Approximate wall boundary conditions in the large eddy simulation of high Reynolds number flow," Flow, Turbulence and Combustion, **63**, 269–291.

[27] Wang M., and Moin P., 2002. "Dynamic wall modeling for large-eddy simulation of complex turbulent flows," Physics of Fluids, **14 (7)**, 2043–2051.

[28] Tessicini F., Li N., and Leschziner M. A., 2007. "Large-eddy simulation of three-dimensional flow around a hill-shaped obstruction with a zonal near-wall approximation," International Journal of Heat and Fluid Flow, **28**, 894-908.

[29] Patil S. S., and Tafti D. K., 2010. "Large-eddy simulation with zonal near wall treatment of flow and hear transfer in a ribbed duct for the internal cooling of turbine blades," ASME Turbo-Expo 2011, Vancouver, Canada, Paper No. GT2011-45749.

[30] Kaltenbach H., Fatica M., Mittal R., Lund T. S., and Moin P., 1999. "Study of flow in a planar asymmetric diffuser using large-eddy simulation," Journal of Fluid Mechanics, **390**, 151-185.

[31] Friedrich R., and Arnal M., 1990. "Analysing turbulent backward-facing step flow with the lowpass-filtered Navier-Stokes equation," Journal of Wind Engineering and its Applications, **35**, 101-128.

[32] Rozati A., and Tafti D. K., 2008. "Large eddy simulation of leading edge film cooling," Journal of Turbomachinery, **130**, 1-7.

[33] Lund T., Wu X., and Squires D., 1998. "Generation of turbulent inflow data for spatially-developing boundary layer simulations," Journal of Computational Physics, **140**, 233-258.

[34] Aider J., and Danet A., 2006. "Large-eddy simulation study of upstream boundary condition influence upon a backward-facing step flow," Comptes Rendus Mecanique, **334**, 447-453.

[35] Wang M., and Moin P., 2000. "Computation of trailing-edge flow and noise using large-eddy simulation," AIAA Journal, **38**, 2201-2209.

[36] Sagaut P., Garnier E., Tromeur E., Larcheveque L., and Labourasse E., 2004. "Turbulent inflow conditions for LES of compressible wall bounded flows," AIAA Journal, **42(3)**, 469-477.

[37] Jarrin N., Benhamadouche S., Laurence D., and Prosser R., 2007. "A synthetic-eddy method for generating inflow conditions for large-eddy simulations," International Journal of Heat and Fluid Flow, **27**, 585-593.

[38] Germano, M., Piomelli, U., Moin, P., and Cabot, W. H., 1991. "A dynamic subgrid-scale eddy viscosity model," Physics of Fluids A, **3**, 1760-1765.

[39] Lilly D. K., 1992. "A proposed modification of the Germano subgrid scale closure method," Physics of Fluids, **A4**, 633-635.

[40] Kays W. M., 1992. "Turbulent Prandtl number – where we are?," Max Jacobs Memorial Award Lecture, 1-12.

[41] Patil S. S., and Tafti D. K., 2011. "Wall modeled large-eddy simulation of flow over a backward facing step with synthetic inlet turbulence," AIAA paper No. 896435, AIAA Aerospace Science Meeting, Orlando, Fl, USA.

[42] Tafti D. K., 2001. "GenIDLEST—A scalable parallel computational tool for simulating complex turbulent flows," In: Proceedings of the ASME Fluids Engineering Division, FED, ASME-IMECE, November 2001, New York, **256**.

[43] Tafti D. K., 2010. "Time-accurate techniques for turbulent heat transfer analysis in complex geometries, Advances in Computational Fluid Dynamics and Heat Transfer;" Eds: Ryo Amano & Bengt Sunden, Series: Developments in Heat Transfer, WIT PRESS, Southampton, UK, in press.

[44] Patil S. S. and Tafti D. K., 2011. "Wall modeled large-eddy simulations of high Reynolds number complex flows with synthetic inlet turbulence," International Journal of Heat and Fluid Flow, submitted.